


Average-atom calculations of bound-free and free-free cross sections in dense plasmasW. R. Johnson ^{*}*Department of Physics, University of Notre Dame, 225 Nieuwland Science Hall, Notre Dame, Indiana 46556, USA*Joseph Nilsen [†]*Lawrence Livermore National Laboratory, Livermore, California 94551, USA* (Received 6 August 2020; revised 12 September 2020; accepted 25 September 2020; published 14 October 2020)

Cross sections for photo-induced bound-free and free-free transitions in plasmas are evaluated in the average-atom approximation and applied to determine opacities of dense plasmas of light elements. Parameters characterizing the plasmas (chemical potential, average ionic charge, free electron density, bound and continuum wave functions, and occupation numbers) are obtained from the average-atom model. Lowest-order calculations of the free-free cross sections, which diverge in the low-frequency limit, are regularized by accounting for the finite electron-ion relaxation time. The resulting analysis provides the basis for average-atom studies of plasma opacities. Such studies are presented for dense lithium, beryllium, boron, and carbon. Applications are given to Rosseland mean opacities of dense hydrogen and deuterium plasmas and to comparisons of free-free to bound-free opacities in shock-compressed plasmas. Average-atom cross section and opacity calculations are extended to plasmas consisting of more than one ionic species, boron nitride, polystyrene, and a composite H, He, C plasma.

DOI: [10.1103/PhysRevE.102.043209](https://doi.org/10.1103/PhysRevE.102.043209)**I. INTRODUCTION**

This paper is devoted to the evaluation of cross sections for absorption of a photon by an electron moving in the field of an ion. The electron and ion are assumed to be components of a plasma described in the average-atom approximation. Bound-free and free-free transitions play important roles in determining the opacity of plasmas, and average-atom models provide a relatively simple yet useful approach to evaluating the associated cross sections and the related opacities. There have been a number of calculations of bound-free cross sections in which an average-atom potential is used to describe the electron-ion interaction [1–5]. Although there have been numerous quantum mechanical calculations of free-free transition cross sections [6–25], only two published calculations [10,20] have employed an average-atom model to describe the electron-ion interaction. In most of the above calculations of free-free cross sections, results are expressed in terms of the Gaunt factor [26]: the ratio of the quantum mechanical to classical (Kramers) free-free cross section [27].

There are two, somewhat different, theoretical approaches to plasma opacities: the first approach which is based on the Lambert-Beers law is used in the opacity tables of Henke [28] and x-ray attenuation tables of Hubbel and Selzer [29]. In this approach the plasma opacity is expressed in terms of bound-free and free-free cross sections. The alternative approach to opacities is based on the Kubo formula for plasma conductivity and was developed by Desjarlais *et al.* [30] within the framework of density-functional theory. This approach

was later adapted to average-atom models in Refs. [31–33]. Inasmuch as the focus of the present paper is on accurate calculations of bound-free and free-free cross sections, we limit our discussion of opacities to those based on cross sections. A recent review of average-atom studies of opacities of dense plasmas is given by Piron and Blenski [34].

In the present paper, we use the average-atom model described in Ref. [31] to determine properties of a plasma including the electron-ion interaction potential and wave functions for bound and continuum electrons moving in this potential. In Sec. II we set out the equations used to evaluate the cross sections and show how the infrared divergence in the free-free cross section is regularized by considering the finite electron-ion relaxation time. Section III, which includes a discussion of the Gaunt factor, is applied to evaluate opacities of dense one-ion and multi-ion plasmas of light elements. An Appendix is included in which an accurate and efficient method is described to evaluate velocity-form matrix elements for the average-atom and similar models where the electron-ion interaction potential has finite range.

II. THEORY**A. Bound-free cross section**

The bound-free (photoionization) cross section for transitions from an ionic bound state $|a\rangle$ to a free-electron state $|b\rangle$ induced by absorption of a photon of frequency ω , evaluated in the unretarded dipole approximation, is

$$\sigma(\omega) = \frac{(2\pi)^2 \alpha \hbar}{m^2 \omega} \int (f_a - f_b) |\langle b | \mathbf{p} \cdot \boldsymbol{\epsilon} | a \rangle|^2 \times \delta(E_b - E_a - \omega) \frac{V d^3 p_b}{(2\pi \hbar)^3}, \quad (1)$$

^{*}johnson@nd.edu[†]jnilsen@llnl.gov

In the above, \mathbf{p} is the momentum operator, $\boldsymbol{\epsilon}$ is the photon polarization vector, and f_a, f_b are Fermi distribution functions

$$f_{a,b} = \frac{1}{1 + \exp[(E_{a,b} - \mu)/kT]}. \quad (2)$$

The bound-state radial wave function $P_a(r)$ is normalized to 1, and the associated occupation number in the average atom approximation is $2(2l_a + 1)f_a$. The factor $(f_a - f_b)$ in Eq. (1) accounts for the partial occupation of state $|a\rangle$ modified to include Pauli blocking. The continuum state wave function is normalized in a box of volume V and behaves asymptotically as a plane wave plus an incoming spherical wave; the associated radial wave function $P_b(r)$ is a phase-shifted cosine wave asymptotically:

$$\lim_{r \rightarrow \infty} P_b(r) = \cos(k_b r - (l + 1)/2 + \delta_b) \quad (3)$$

with $k_b = p_b/\hbar$. After summing over magnetic quantum numbers and spins of electrons, averaging over photon polarization directions and integrating over free-electron directions, Eq. (1) becomes

$$\sigma = \frac{16\pi}{3} \alpha \frac{m}{p_b} \sum_a (f_a - f_b) S_{ba}, \quad (4)$$

where the sum extends over all bound states a in the average atom. In the above,

$$S_{ba} = l_a |M_{l_a-1, l_a}|^2 + (l_a + 1) |M_{l_a+1, l_a}|^2, \quad (5)$$

with

$$\begin{aligned} M_{l_a-1, l_a} &= \int_0^\infty dr P_{\epsilon_b, l_a-1}(r) \left(\frac{d}{dr} + \frac{l_a}{r} \right) P_{\epsilon_a, l_a}(r), \\ M_{l_a+1, l_a} &= \int_0^\infty dr P_{\epsilon_b, l_a+1}(r) \left(\frac{d}{dr} - \frac{l_a+1}{r} \right) P_{\epsilon_a, l_a}(r). \end{aligned} \quad (6)$$

Although it is common practice in studies of photoionization to replace the above velocity-form matrix elements by length form matrix elements, it is more convenient to treat contributions from the region $r > R_{WS}$, the radius of the Wigner-Seitz sphere containing the ion, analytically using Eqs. (6).

B. Free-free cross section

The free-free (inverse bremsstrahlung) cross section for transitions from a free-electron state $|a\rangle$ to a free-electron state $|b\rangle$ moving in the field of an ion and evaluated in the unretarded dipole approximation, is

$$\begin{aligned} \sigma(\omega) &= \frac{(2\pi)^2 \alpha \hbar}{m^2 \omega} \int (f_a - f_b) |\langle b | \mathbf{p} \cdot \boldsymbol{\epsilon} | a \rangle|^2 \\ &\quad \times \delta(E_b - E_a - \hbar\omega) \frac{d^3 p_a V}{(2\pi \hbar)^3} \frac{d^2 p_b V}{(2\pi \hbar)^3}. \end{aligned} \quad (7)$$

The incident and final state wave functions behave asymptotically as plane waves plus outgoing and incoming spherical waves, respectively. As for bound-free transitions, the associated radial wave functions $P_a(r)$ and $P_b(r)$ approach phase-shifted cosine waves asymptotically. Summing over electron magnetic quantum numbers and spins, averaging over photon polarization directions, and integrating over electron

directions, one obtains

$$\sigma(\omega) = \int (f_a - f_b) \sigma(p_a, \omega) dn_a, \quad (8)$$

where the differential free-electron density is

$$dn_a = \frac{p_a^2 dp_a}{\pi^2 \hbar^3}. \quad (9)$$

It should be noted that

$$\int_0^\infty f_a dn_a = n_e = Z^* n_{\text{ion}}, \quad (10)$$

where n_{ion} and n_e are the ion and electron number densities, respectively, and Z^* is the mean ionic charge predicted by the average-atom theory. Again, the factor $(f_a - f_b)$ in Eq. (8) accounts for Pauli blocking of transitions from initial free-electron states. The function $\sigma(p_a, \omega)$ in Eq. (8) is

$$\sigma(p_a, \omega) = \frac{32\pi^2}{3} \alpha \left(\frac{mc^2}{\hbar\omega} \right) \left(\frac{\hbar}{mc} \right)^2 \frac{\hbar^3}{p_a^2 p_b} S_{ba}. \quad (11)$$

In the above,

$$S_{ba} = \sum_{l_a=0}^{\infty} [l_a |M_{l_a-1, l_a}|^2 + (l_a + 1) |M_{l_a+1, l_a}|^2], \quad (12)$$

where the velocity-form matrix elements are given by Eqs. (6). Although nonrelativistic free-free matrix elements are typically evaluated in acceleration form, it is much simpler here, as for bound-free transitions, to develop formulas for the contribution from $r > R_{WS}$ using velocity-form matrix elements.

C. Free-free infrared divergence

The velocity-form matrix elements M_{ba} in Eq. (6) are proportional to $1/\omega$ and $f_a - f_b$ is proportional to ω in the $\omega \rightarrow 0$ limit; therefore, the free-free cross section $\sigma(\omega)$ diverges as ω^{-2} as ω approaches 0. This is a well-understood infrared divergence associated with the single-ion approximation to the electron-ion interaction. A method to regularize the infrared divergence for the closely related average-atom implementation of the Kubo-Greenwood formula [31] was discussed in Refs. [35,36]. This regularization requires that account be taken of the time between successive electron-ion collisions in the plasma.

Following the arguments given in Refs. [35,36], one finds that as $\omega \rightarrow 0$,

$$\sigma(p_a, \omega) \rightarrow \frac{4\pi}{3} \alpha \frac{p_a^3}{m^3 \omega^3} \sigma_{\text{tr}}(p_a), \quad (13)$$

where $\sigma_{\text{tr}}(p)$ is the transport cross section, which is given in terms of the elastic-scattering form factor $f(p)$ as

$$\begin{aligned} \sigma_{\text{tr}}(p) &= \int (1 - \cos \theta) |f(q)|^2 d\Omega \\ &= \frac{4\pi \hbar^2}{p^2} \sum_{l=0}^{\infty} (l+1) \sin^2[\delta_{l+1}(p) - \delta_l(p)]. \end{aligned} \quad (14)$$

Equation (13) is in agreement with the limiting value of the low-frequency approximation obtained in Eq. (36) of

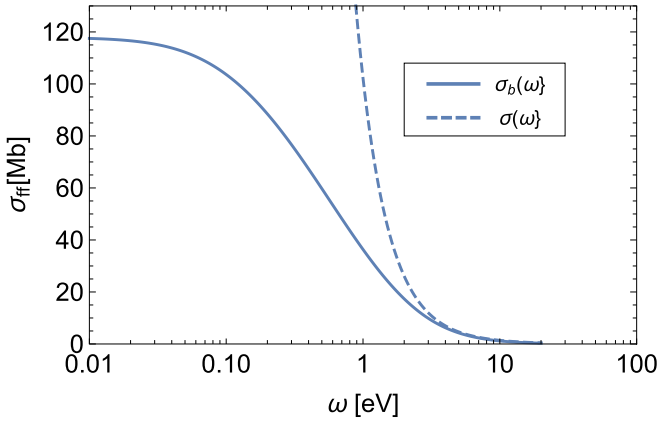


FIG. 1. The regularized free-free cross section $\sigma_b(\omega)$ for Li at density $\rho = 0.534$ g/cc and temperature $T = 2$ eV shown in the solid line is compared with the infrared divergent cross section $\sigma(\omega)$ shown in the dashed line

Ref. [21]. In the low-frequency limit,

$$f_a - f_b \xrightarrow{\omega \rightarrow 0} -\hbar\omega \frac{df}{dE}, \quad (15)$$

and one can combine Eqs. (13) and (15) to obtain the following low-frequency approximation to the free-free cross section

$$\sigma(\omega) \approx \frac{16\alpha}{3\pi\hbar^2\omega^2} \int \left(-\frac{df}{dE}\right) E^2 \sigma_{\text{tr}}(p) dE, \quad (16)$$

which clearly isolates the infrared divergence.

The mean-free path in a plasma is $\Lambda = 1/[n_{\text{ion}}\sigma_{\text{tr}}(p)]$, and the corresponding relaxation time is

$$\tau(p) = \Lambda/v = m/[pn_{\text{ion}}\sigma_{\text{tr}}(p)]. \quad (17)$$

As discussed in Ref. [35], the effect of the finite relaxation time is to replace ω by $\omega - i/\tau(p)$ in the transition matrix element or equivalently

$$\omega^2 \rightarrow \omega^2 + \tau(p)^{-2} \quad (18)$$

in the cross section. The resulting low-frequency cross section is

$$\sigma_b(\omega) = \frac{16\alpha}{3\pi\hbar^2} \int \left(-\frac{df}{dE}\right) E^2 \frac{\sigma_{\text{tr}}(p)}{\omega^2 + \tau(p)^{-2}} dE. \quad (19)$$

The above arguments, when applied to the Kubo-Greenwood expression for conductivity, lead to a frequency-dependent generalization of the Ziman conductivity formula [37,38].

The free-free cross section $\sigma(\omega)$ is compared with its divergence-free counterpart $\sigma_b(\omega)$ in Fig. 1 for Li at $T = 2$ eV. For the light elements considered herein, as illustrated for Li in Fig. 1, the regularized and divergent cross sections differ noticeably only for frequencies $\omega < 10$ eV, so the modifications discussed in this section have little or no influence on the examples shown later.

III. OPACITIES

A. Basic definitions

The opacity μ of a medium is defined through the Lambert-Beer law: the reduction in intensity of a beam as it passes a

distance through a medium is proportional to the intensity,

$$dI = -\mu\rho I(x) dx, \quad (20)$$

where ρ is the density of the medium. For bound-free and free-free absorption of a photon beam of frequency ω by electrons in a plasma, considered here, the reduction in intensity can be expressed alternatively in terms of the absorption cross sections:

$$dI = -(\sigma_{\text{bf}} + \sigma_{\text{ff}}) n_{\text{ion}} I(x) dx, \quad (21)$$

where n_{ion} is the ion number density. This permits one to express the opacity μ in terms of the absorption cross sections:

$$\mu_{\text{bf, ff}}(\omega) = \sigma_{\text{bf, ff}}(\omega) n_{\text{ion}}/\rho. \quad (22)$$

The Rosseland mean opacity $\langle\mu\rangle$, important in astrophysical applications, is defined by

$$\frac{1}{\langle\mu\rangle} = \frac{\int_0^\infty \frac{1}{\mu(\nu)} \frac{\partial B_\nu}{\partial T} d\nu}{\int_0^\infty \frac{\partial B_\nu}{\partial T} d\nu}, \quad (23)$$

where

$$B_\nu = \frac{2\pi}{c^2} \frac{\nu^3}{(e^{h\nu/kT} - 1)} \quad (24)$$

is the Planck distribution function and, correspondingly,

$$\frac{1}{k} \frac{\partial B_\nu}{\partial T} = \frac{2\pi h\nu^4 e^{h\nu/kT}}{c^2 (kT)^2 (e^{h\nu/kT} - 1)^2}. \quad (25)$$

The integral in the denominator of Eq. (23) is

$$\int_0^\infty \frac{1}{k} \frac{\partial B_\nu}{\partial T} d\nu = \frac{8\pi^5 (kT)^3}{15c^2 h^4}. \quad (26)$$

It follows that

$$\frac{1}{\langle\mu\rangle} = \frac{15}{4\pi^4} \int_0^\infty \frac{1}{\mu(x)} \frac{x^4 e^x}{(e^x - 1)^2} dx, \quad (27)$$

where $x = h\nu/kT$.

B. Gaunt factor and Kramers cross section

The classical Kramers free-free cross section [see, for example, Eq. (16) of Ref. [21]] is

$$\sigma_K(p_a, \omega) = \frac{16\pi^3}{3\sqrt{3}} \alpha \frac{(\alpha Z^*)^2 \hbar^2 c^2}{m p_a \omega^3}. \quad (28)$$

As alluded to in the introduction, it is common to express the corresponding quantum mechanical cross section $\sigma(p_a, \omega)$ in terms of the classical Kramers cross section. The (dimensionless) Gaunt factor, which is often used in tabulations of $\sigma(p_a, \omega)$, is the ratio of the quantum mechanical to classical cross section,

$$G(p_a, \omega) = \frac{\sigma(p_a, \omega)}{\sigma_K(p_a, \omega)} = \frac{2\sqrt{3}}{\pi(\alpha Z^*)^2} \frac{k^2}{k_a k_b} S_{ba}, \quad (29)$$

where $k_a = p_a/\hbar$, $k_b = p_b/\hbar$, and $k = \omega/c$. In the above, Z^* is the average ionic charge of the plasma.

The classical counterpart of the free-free cross section $\sigma(\omega)$ is obtained by integrating $\sigma_K(p_a, \omega)$ over the electron

distribution:

$$\sigma_K(\omega) = \frac{1}{\pi^2 \hbar^3} \int_0^\infty (f_a - f_b) \sigma_K(p_a, \omega) p_a^2 dp_a. \quad (30)$$

Traditionally, the Maxwell-Boltzmann distribution rather than the Fermi distribution is used for $f_{a,b}$ leading to a version of the Kramers cross section modified to account for Pauli blocking:

$$\sigma_K(\omega) = \frac{16\pi^2 \alpha^3}{3} \sqrt{\frac{2\pi}{3mkT}} \frac{(Z^*)^2 \hbar^2 c^2}{m\omega^3} n_e (1 - e^{-\hbar\omega/kT}). \quad (31)$$

The reciprocal of Kramers' cross section may be written

$$\frac{1}{\sigma_K} = \frac{(mkT)^{7/2}}{\alpha^2 c^2 \hbar^2 m^2 (Z^*)^2 n_e} \frac{x^3}{1 - e^{-x}}, \quad (32)$$

where $x = \hbar\nu/kT$. The Rosseland mean cross section is

$$\frac{1}{\langle \sigma_K \rangle} = \frac{(mkT)^{7/2}}{\alpha^2 c^2 \hbar^2 m^2 (Z^*)^2 n_e} \frac{15}{4\pi^4} \int_0^\infty \frac{x^7 e^x}{(e^x - 1)^2 (1 - e^{-x})}. \quad (33)$$

The integral above evaluates to 5104.745 and the resulting Rosseland mean cross section is

$$\langle \sigma_K \rangle = d_K \frac{\alpha^2 c^2 \hbar^2 m^2 (Z^*)^2 n_e}{(mkT)^{7/2}}, \quad (34)$$

where the dimensionless constant $d_K = 0.00282870$. In atomic units $m = 1$, $\hbar = 1$, $c = 1/\alpha$, one obtains

$$\langle \mu_K \rangle = d_k (kT)^{-7/2} (Z^*)^2 n_e n_{\text{ion}} / \rho, \quad (35)$$

for the Rosseland mean of the Kramers opacity.

C. Dense plasmas of light metal elements

As a first example, average-atom calculations of opacities of Li, Be, B, and C at temperature $T = 10$ eV and densities $\rho = 0.534, 1.848, 2.463, 2.268$ g/cc, respectively, in the frequency range $\omega = 10$ –1000 eV are presented in Fig. 2. The $1s$ state, which is fully occupied, is the only bound state in these plasmas at $T = 10$ eV, so there are no bound-bound contributions to the opacity. For photon energies below the $1s$ photoionization threshold only free-free absorption, shown by the blue line, contributes to the opacity. Above the threshold, photoionization of $1s$ electrons dominates the opacity. The solid red lines in Fig. 2 show the average-atom bound-free contribution to the opacity. The black dots joined by the thin black line in Fig. 2 are experimental data from pp. 215–217 of Ref. [28]. Sources of the experimental data for each element are listed at the bottom of the corresponding page in [28]. It is interesting to note how well the relatively simple average atom picture tracks the cold-matter experimental data.

D. Dense hydrogen and deuterium plasmas

As a second application of the present formalism, we evaluate the contribution of free-free absorption to the Rosseland mean opacity of dense hydrogen and deuterium plasmas, where bound-free absorption plays no role. We, of course, ignore the contribution of Thompson scattering here. The solid green, orange, and blue lines in Fig. 3 show the opacities

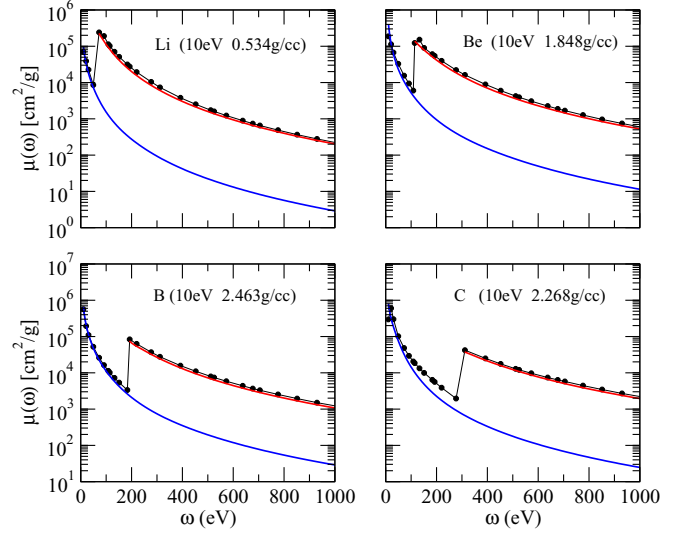


FIG. 2. Average-atom contributions of free-free and bound-free contributions to opacities are illustrated by the blue and red curves, respectively. The black dots joined by the thin blue line are experimental data from Ref. [28].

of hydrogen plasmas at densities 1, 10, and 200 g/cc, respectively. Differences between the solid curves reflect differences in n_{ion} and n_e associated with differences in plasma mass densities. The dashed green, orange, and blue lines in the

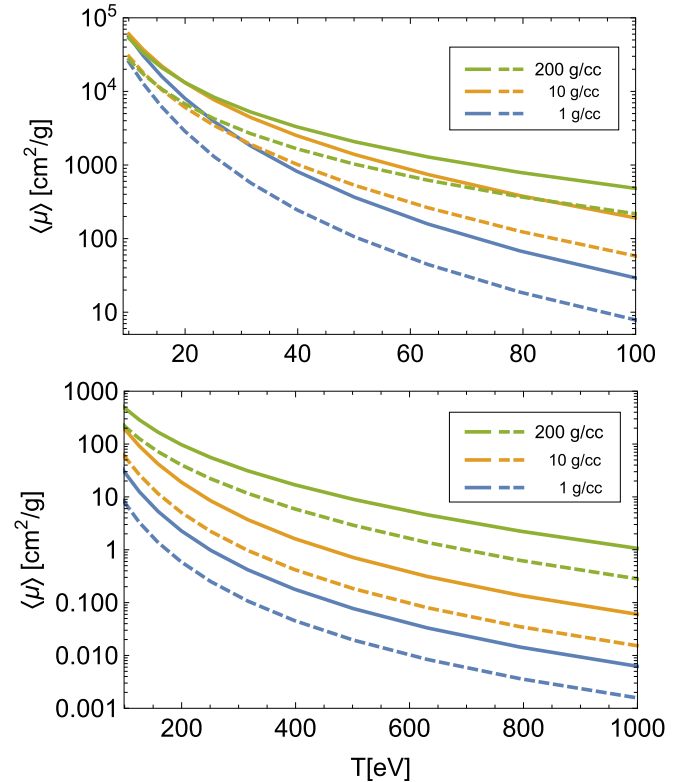


FIG. 3. Rosseland mean opacities for dense hydrogen and deuterium plasmas as functions of temperature. The solid lines show the hydrogen opacities for plasma densities $\rho = 1, 10,$ and 200 g/cc. The dashed lines show the opacities at these densities for deuterium.

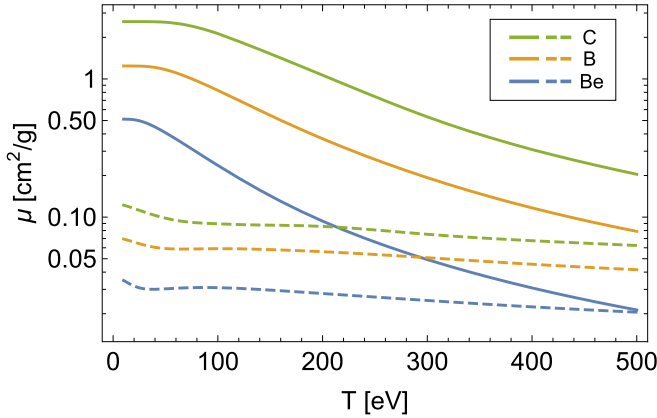


FIG. 4. Solid and dashed lines show bound-free and free-free contributions, respectively, to the opacity at $\omega = 9$ keV of four times compressed Be, B, and C. The bound-free contributions are seen to be decreasing functions of temperature whereas the free-free contributions become independent of T as temperature increases.

figure show the Rosseland mean opacities of deuterium plasmas at densities 1, 10, and 200 g/cc, respectively. Differences between the H and D curves at fixed density reflect differences in n_{ion} owing to the difference in atomic weights.

E. Shock-compressed plasmas

A shock wave passing through a plasma can compress matter behind the shock front by a factor of approximately 4 near the peak of the Hugoniot curve. In recent experiments [39–42] conditions behind the shock fronts were probed by a He-like Zn K-x-ray at $\omega = 9$ keV. In these experiments the dominant contribution to the opacity at the probe energy was from bound-free absorption which is approximately proportional to the K-shell occupation number. For precise measurements of properties of a shock-compressed plasma it is necessary to account for free-free absorption. The role of free-free transitions in the opacity of shock-compressed light element plasmas is illustrated in Fig. 4, where free-free and bound-free opacities for four times compressed Be, B, and C are shown as functions of temperature at $\omega = 9$ keV. The bound-free opacity decreases with temperature, while the free-free cross section is relatively flat leading to the increasing importance of free-free transitions with temperature. Indeed, at $\omega = 9$ keV free-free transitions dominate the opacity of four times compressed Li plasmas for $T > 300$ eV and four times compressed Be plasmas for temperatures $T > 500$ eV.

In Fig. 5 free-free contributions to the opacity of four times compressed boron at $\omega = 9$ keV from the present average-atom calculation are compared with calculations based on the phase amplitude method [10] and with calculations based on the Karzas-Latter [23] theory shown in Ref. [43]. The phase-amplitude method is described in Ref. [10], whereas the Karzas-Latter results come from a calculation with an effective ion charge from the detailed configuration accounting model described in Refs. [44,45]. For comparison purposes, we show the present average-atom results and results from the classical Kramers [27] theory evaluated using average-atom electron densities. The disagreement between

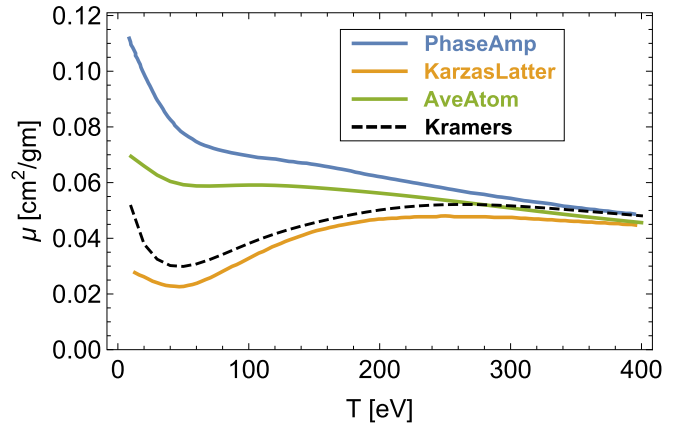


FIG. 5. Free-free contributions to the opacity of four times compressed boron at $\omega = 9$ keV from phase-amplitude and Karzas-Latter calculations in Ref. [43] are compared with the present average-atom opacity for temperatures ranging from 10 to 400 eV. The dashed black line shows the opacity obtained from the Kramers classical cross section.

the Karzas-Latter theory and the average-atom theory opacities is expected; the Karzas-Latter cross section describes scattering from an unscreened ion of charge Z^* whereas the average-atom model describes scattering from a screened ion with effective charge Z^* . The difference between the phase-amplitude and average-atom calculations is more difficult to understand. The bound-free contributions to opacity for all three quantum mechanical calculations are in close agreement as shown in Ref. [43] indicating that all three methods are using similar ionization states as a function of temperature. The differences in the average-atom and phase-amplitude opacities are therefore most likely to arise from differences in free-free cross sections and not from the plasma models used to describe the electron-ion potential.

F. Applications to composite plasmas

To treat composite plasmas, such as boron-nitride BN or polystyrene C_8H_8 , we adjust the densities of individual ions to ensure that the WS volume of the composite is the sum of the WS volumes of its components. Thus for a plasma having fractional occupation x_i for ions with atomic weight A_i and density ρ_i ,

$$\frac{\sum_i x_i A_i}{N_A \rho} = \sum_i \frac{x_i A_i}{N_A \rho_i}, \tag{36}$$

where N_A is Avogadro’s number and ρ is the plasma density. The above relation provides one equation for n unknown densities ρ_i . The free-electron densities $n_e(i)$ associated with different types of ion in the plasma must also be identical, leading to the remaining $n - 1$ equations

$$n_e(1) = n_e(2) = n_e(3) = \dots = n_e(n) \tag{37}$$

needed to determine the densities of component ions. It should be noted that the above equation ensures that the chemical potential is a plasma property, independent of the type of ion. The opacity of the composite plasma is the weighted sum of

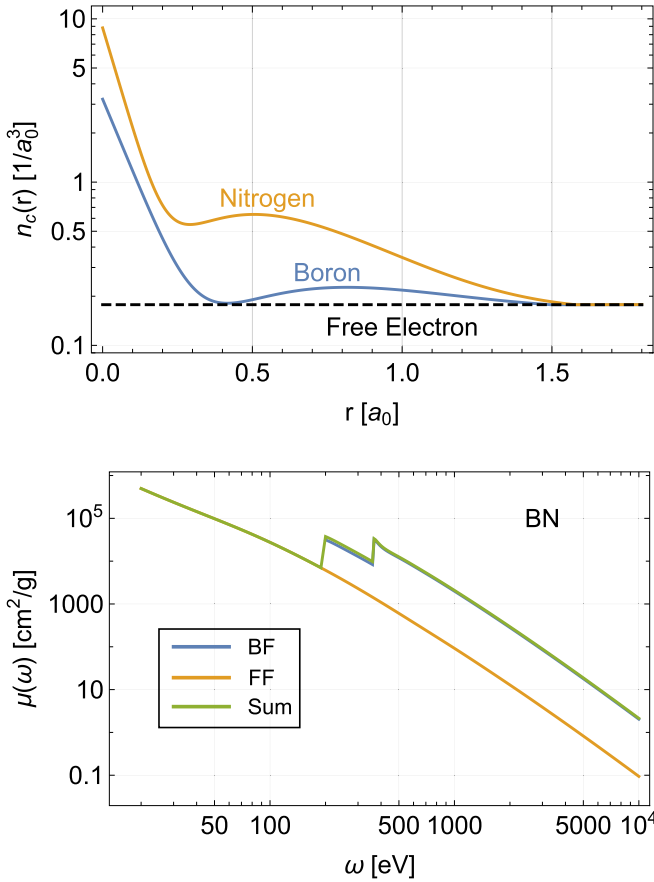


FIG. 6. Upper panel: Continuum densities $n_c(r)$ for boron and nitrogen in a BN plasma at $T = 20$ eV and $\rho = 9.21$ g/cc are shown inside the respective WS spheres. The densities converge to the free-electron density at ionic boundaries. Lower panel: Contributions to the opacity of the BN plasma described in the upper panel.

the opacities of its components:

$$\mu = \sum_i x_i \mu_i. \quad (38)$$

In the upper panel of Fig. 6 densities of continuum electrons $n_c(r)$ inside the WS spheres of B and N ions in compressed BN at $T = 20$ eV and $\rho = 9.12$ g/cc are shown. The WS radii of B and N are $1.50a_0$ and $1.58a_0$, respectively. The continuum densities are seen to converge to the constant free-electron density n_e at the respective WS boundaries. The $1s$ shell is fully occupied for both ions, whereas all other shells are empty. Bound-free and free-free contributions to the opacity of the BN plasma are shown in the lower panel of Fig. 6 as functions of photon frequency ω . The green line shows the sum of the free-free (FF) and bound-free (BF) contributions. The orange curve shows the FF opacity, which is the only contribution to the sum below the boron K-shell photoionization threshold. The bound-free contribution, shown in blue, can be seen in the interval between the B and N thresholds but is masked by the green line above the N threshold.

The corresponding plot for a polystyrene C_8H_8 plasma at density 4.24 g/cc ($4\rho_0$) is shown in the upper panel of Fig. 7. Inasmuch as H is completely ionized, the BF contribution to the opacity is from C ions only. In the lower panel of Fig. 7

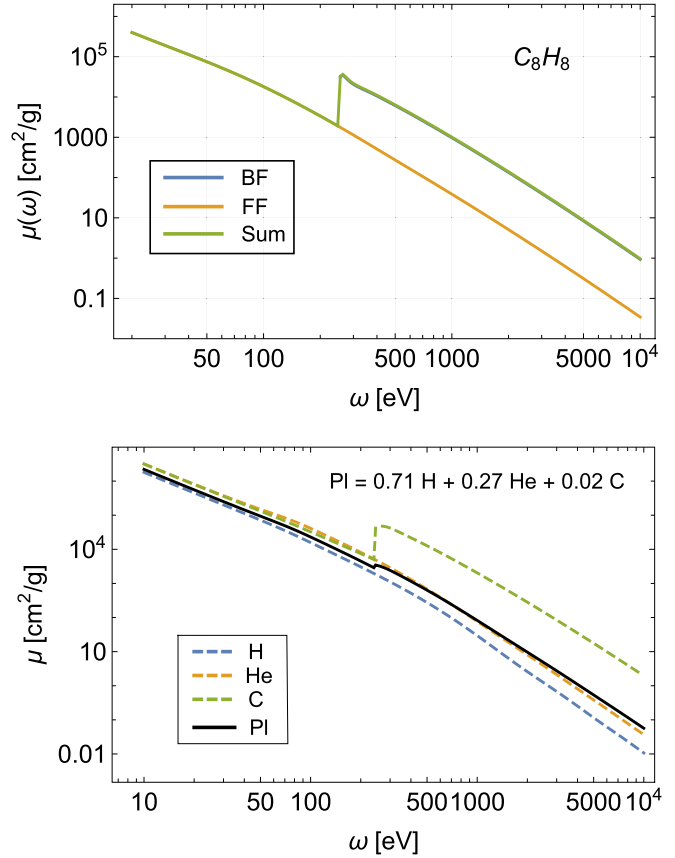


FIG. 7. Upper panel: Contributions to the opacity of a C_8H_8 plasma at $T = 20$ eV and $\rho = 4.24$ g/cc. Lower panel: Contributions to the opacity of a H, He, C plasma with concentrations 0.71, 0.27, 0.02, respectively, at $T = 20$ eV and $\rho = 10$ g/cc.

the opacity of a plasma consisting of H, He, and C ions is illustrated. The relative concentrations are taken to be 0.71, 0.27, and 0.02, respectively, from observational constraints on brown dwarf stars listed in Table 1 of Ref. [46].

IV. SUMMARY

Bound-free and free-free photoabsorption cross sections are studied in the average-atom approximation and applied to determine the corresponding contributions to opacities of light-element plasmas. The infrared divergence in the free-free cross section is regularized by taking account of the finite electron-ion relaxation time leading to a finite $\omega = 0$ limit and found to significantly modify cross sections of light element plasmas for $\omega < 10$ eV.

Bound-free and free-free contributions to opacity $\mu(\omega)$ are expressed in terms of bound-free and free-free cross sections and the frequency-averaged Rosseland mean opacity $\langle \mu(\omega) \rangle$ is introduced. The average-atom expression for the Gaunt-factor is given together with the related classical (Kramers) expression for the free-free cross section. An analytic expression for the Rosseland mean of the Kramers opacity, which is useful for comparison purposes, is also given.

As a first example of the present formalism, applications are given to dense plasmas of light elements at temperature $T = 10$ eV for photon energies $\omega = 10$ –1000 eV.

The average-atom opacities for these elements are compared with cold-matter experimental data tabulated in Ref. [28].

In a second example, Rosseland mean opacities of H and D plasmas at densities 1, 10, and 200 g/cc are compared over a temperature range from $T = 10$ to 1000 eV. Differences in opacities for these hydrogen plasmas at different densities can be traced to differences in ion densities, which in the average-atom model are reciprocals of the corresponding Wigner-Seitz cell volumes. Differences between the opacities of H and D, both of which have nuclear charge $Z = 1$, are the result of a factor of 2 decrease in n_{ion} for D compared with H at a given mass density.

A third example concerns four times compressed light elements. The free-free and bound-free opacities are evaluated as functions of temperature for $\omega = 9$ keV to illustrate the increasingly important role of free-free transitions with temperature. Comparison of the $\omega = 9$ keV free-free opacity of compressed boron from average-atom calculations with the phase amplitude method and Karzas-Latter calculations show surprisingly large differences in the temperature range 10 to 400 eV in view of the excellent agreement noted in Ref. [43] of the corresponding bound-free opacities.

As final examples, opacities of composite BN, CH, and H-He-C plasmas are studied in the average-atom approximation.

All calculations are carried out using velocity-form matrix elements. Radial matrix elements are evaluated using standard point-by-point numerical integration for r smaller than the Wigner-Seitz cell radius and matched to values for larger r determined analytically.

ACKNOWLEDGMENTS

The authors owe debts of gratitude to Carlos Iglesias and Daniel Åberg for comparison data and to Mandy Bethkenhagen for useful suggestions and comments on the manuscript. The work of J.N. was performed under the auspices of the U.S. Department of Energy by Lawrence Livermore National Laboratory under Contract DE-AC52-07NA27344.

APPENDIX: COMPUTATIONAL CONSIDERATIONS

In this Appendix we describe the combined numerical-analytical procedure used here to avoid difficulties that arise in when evaluating wave functions using purely numerical methods. A typical example of such difficulties occurs in numerical studies of bound-free transitions for large values of ω , where there is strong cancellation between rapidly oscillating contributions to the matrix element from the region $r < R_{\text{WS}}$ and the region $r > R_{\text{WS}}$. Although it is relatively simple to control the accuracy of the contribution to the matrix element for $r < R_{\text{WS}}$ by choosing a narrowly spaced grid, it is significantly more difficult to control the accuracy of the contribution for $r > R_{\text{WS}}$ using point by point integration. This problem is illustrated in Fig. 8. The dipole matrix element which is the smoothly varying function of frequency shown by the black line in the figure is the sum of two rapidly oscillating functions from $r < R_{\text{WS}}$ shown by the blue line and from the region $r > R_{\text{WS}}$ shown by the orange line. Assuming that the contribution from $r < R_{\text{WS}}$ can be evaluated precisely, it is

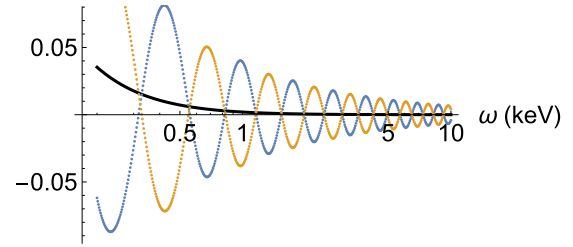


FIG. 8. The dipole matrix element between a weakly bound $2s$ state and a continuum state in a boron plasma at density $\rho = 2.463$ g/cc and temperature $T = 100$ eV is shown. The blue curve is the numerically evaluated contribution to the matrix element from $r < R_{\text{WS}}$. The orange curve is the contribution from $r > R_{\text{WS}}$. The solid black curve is the sum of contributions from the two regions.

clear from Fig. 8 that the contribution from $r > R_{\text{WS}}$ must also be evaluated with exquisite precision to produce the smooth sum shown by the black line. In the average-atom theory, where the potential vanishes beyond R_{WS} , wave functions for both bound states and free-particle states are well known analytically and contributions to matrix elements from the region $r > R_{\text{WS}}$ can be evaluated analytically with the required high precision.

1. Bound-state wave functions

In the region $r < R_{\text{WS}}$, the bound-state wave function is determined numerically using point-by-point numerical integration. Beyond the WS radius, the potential vanishes in the average-atom approximation and the radial wave function for a bound state with energy $-\epsilon$ and angular momentum l is

$$P_{\ell l}(r) = A\lambda r k_l(\lambda r), \quad (\text{A1})$$

where, in atomic units, $\lambda = \sqrt{-2\epsilon}$ and where A is a constant determined by matching Eq. (A1) to the wave function $P_{\ell l}(r)$, which is determined by numerical integration, at the WS boundary. The function $k_l(x)$ in Eq. (A1) is a modified spherical Bessel function. The normalization of the modified spherical Bessel functions used here differs by a factor of $\pi/2$ from the functions $k_l(z)$ defined in Ref. [47]. Specifically, we define

$$k_0(z) = e^{-z}/z, \quad (\text{A2})$$

$$k_1(z) = e^{-z}(1/z + 1/z^2), \quad (\text{A3})$$

$$k_2(z) = e^{-z}(1/z + 3/z^2 + 3/z^3). \quad (\text{A4})$$

The functions $k_l(z)$ for $l > 2$ can be obtained from the recursion relation

$$k_{l+1}(z) = k_{l-1}(z) + [(2l+1)/z]k_l(z). \quad (\text{A5})$$

2. Continuum wave functions

Two independent solutions to the radial Schrödinger equation for $p = \sqrt{2\epsilon}$ (in atomic units) are $P_l(r) = pr j_l(pr)$ and $P_l(r) = pr y_l(pr)$, where j_l and y_l are spherical Bessel and Neumann functions, respectively. The general solution to the radial equation in the field-free region may be written as a

linear combination of the two independent solutions:

$$P_l(r) = pr j_l(pr) \cos \delta_l - pr y_l(pr) \sin \delta_l. \quad (\text{A6})$$

This solution has the asymptotic limit

$$\lim_{r \rightarrow \infty} P_l(r) = \cos \left[pr + \delta_l - (l+1) \frac{\pi}{2} \right] \quad (\text{A7})$$

and leads to the interpretation of δ_l as the continuum phase shift.

We integrate the radial Schrödinger equation outward from the origin to the cavity boundary $r = R$ and match the solution and its derivative to a linear combination of the corresponding free-particle radial wave function and its derivative:

$$P_l(R) = N_l [x j_l(x) C_l - x y_l(x) S_l], \quad (\text{A8})$$

$$\frac{1}{p} Q_l(R) = N_l \left\{ \frac{d[x j_l(x)]}{dx} C_l - \frac{d[x y_l(x)]}{dx} S_l \right\}, \quad (\text{A9})$$

where $Q_l(r) = dP_l(r)/dr$ and $x = pr$. The constants S_l and C_l are constants to be determined. Solving, we find

$$N_l S_l = \frac{d[x j_l(x)]}{dx} P_l(R) - x j_l(x) \frac{1}{p} Q_l(R), \quad (\text{A10})$$

$$N_l C_l = \frac{d[x y_l(x)]}{dx} P_l(R) - x y_l(x) \frac{1}{p} Q_l(R). \quad (\text{A11})$$

With the definitions

$$\tan \delta_l = \frac{S_l}{C_l}, \quad N_l = \frac{1}{\sqrt{S_l^2 + C_l^2}}, \quad (\text{A12})$$

the resulting wave function has the desired asymptotic limit. Thus, in the continuum case, as in the bound case, we have numerical wave functions for $r < R_{WS}$ and analytical wave functions for $r > R_{WS}$.

3. Free-free matrix elements

The radial matrix elements for free-free transitions take the form

$$R(bl-1, al) = \int_0^\infty dr P_{bl-1}(r) \left(\frac{d}{dr} + \frac{l}{r} \right) P_{al}, \quad (\text{A13})$$

$$R(bl-1, al) = \int_0^\infty dr P_{bl+1}(r) \left(\frac{d}{dr} - \frac{l+1}{r} \right) P_{al}. \quad (\text{A14})$$

Note first that for free-particle functions, $P_l(x) = x j_l(x)$ or $x y_l(x)$,

$$\left(\frac{d}{dx} + \frac{l}{x} \right) P_l(x) = P_{l-1}(x), \quad (\text{A15})$$

$$\left(\frac{d}{dx} - \frac{l+1}{x} \right) P_l(x) = -P_{l+1}(x). \quad (\text{A16})$$

Thus, the following two cases must be considered for the contribution to the radial integral from $r > R$:

$$\begin{aligned} \Delta R(bl \pm 1, al) = \mp p_a^2 p_b \int_R^\infty r^2 dr [j_{l \pm 1}(p_b r) \cos \delta_b \\ - y_{l \pm 1}(p_b r) \sin \delta_b] [j_{l \pm 1}(p_a r) \cos \delta_a \\ - y_{l \pm 1}(p_a r) \sin \delta_a]. \end{aligned} \quad (\text{A17})$$

The above integrals can be evaluated with the aid of the Lommel integral formula [48,49]. Consider two spherical Bessel

functions (of first or second kind) $f_l(p_a r)$ and $g_l(p_b r)$. These satisfy

$$r^2 \frac{d^2 f_l}{dr^2} + 2r \frac{df_l}{dr} + [p_a^2 r^2 - l(l+1)] f_l = 0, \quad (\text{A18})$$

$$r^2 \frac{d^2 g_l}{dr^2} + 2r \frac{dg_l}{dr} + [p_b^2 r^2 - l(l+1)] g_l = 0. \quad (\text{A19})$$

Multiplying the second of these by f_l and the first by $-g_l$ and adding, we find

$$\frac{d}{dr} \left[f_l \left(f_l \frac{dg_l}{dr} - g_l \frac{df_l}{dr} \right) \right] + (p_b^2 - p_a^2) r^2 f_l g_l = 0.$$

The resulting version of the Lommel formula is

$$\begin{aligned} \int_R^\infty dr r^2 f_l(p_a r) g_l(p_b r) = \frac{R^2}{p_a^2 - p_b^2} \left[g_l(p_b R) \frac{df_l(p_a R)}{dr} \right. \\ \left. - f_l(p_a R) \frac{dg_l(p_b R)}{dr} \right]_{r=R}. \end{aligned} \quad (\text{A20})$$

In the above, we introduced an infinitesimal exponential damping to eliminate the contribution from the upper limit. With the aid of the above, one finds

$$\begin{aligned} \Delta R(bl \pm 1, al) = \mp \frac{p_a^2 p_b R^2}{p_a^2 - p_b^2} \\ \times \{ [j_{l \pm 1}(p_b R) \cos \delta_b - y_{l \pm 1}(p_b R) \sin \delta_b] \\ \times \frac{d}{dr} [j_{l \pm 1}(p_a R) \cos \delta_a - y_{l \pm 1}(p_a R) \sin \delta_a]_R \\ - \frac{d}{dr} [j_{l \pm 1}(p_b R) \cos \delta_b - y_{l \pm 1}(p_b R) \sin \delta_b]_R \\ \times [j_{l \pm 1}(p_a R) \cos \delta_a - y_{l \pm 1}(p_a R) \sin \delta_a] \}. \end{aligned} \quad (\text{A21})$$

To check the numerical evaluation of the above formulas, one can verify that the radial integrals vanish term by term when ionic wave functions are replaced by free-particle wave functions!

4. Bound-free matrix elements

The radial matrix elements for bound-free transitions are given by Eqs. (A13)–(A14) where $P_{al}(r) = A \lambda r k_l(\lambda r)$ and Eqs. (A15) and (A16) are satisfied with the exception that right-hand side of Eq. (A15) is $-P_{l-1}(x)$. The resulting contribution to the radial integral from $r > R$ is

$$\begin{aligned} \Delta R(bl \pm 1, \lambda l) = -A \lambda^2 p_b \int_R^\infty r^2 dr [j_{l \pm 1}(p_b r) \cos \delta_b \\ - y_{l \pm 1}(p_b r) \sin \delta_b] k_{l \pm 1}(\lambda r). \end{aligned} \quad (\text{A22})$$

In the counterpart to Eqs. (A18) and (A19), one replaces $f_l(p_a r)$ by $k_l(\lambda r)$ and p_a^2 by $-\lambda^2$ leading to

$$\begin{aligned} \int_R^\infty dr r^2 g_l(p_b r) k_l(\lambda r) = -\frac{R^2}{\lambda^2 + p_b^2} \left[g_l(p_b R) \frac{dk_l(\lambda R)}{dr} \right. \\ \left. - k_l(\lambda R) \frac{dg_l(p_b R)}{dr} \right]_{r=R}. \end{aligned} \quad (\text{A23})$$

The above steps lead to

$$\Delta R(bl \pm 1, \lambda l) = \frac{A\lambda^2 p_b R^2}{\lambda^2 + p_b^2} \{ [j_{l \pm 1}(p_b R) \cos \delta_b - y_{l \pm 1}(p_b R) \sin \delta_b] \frac{dk_l(\lambda r)}{dr} \Big|_R - \frac{d}{dr} [j_{l \pm 1}(p_b r) \cos \delta_b - y_{l \pm 1}(p_b r) \sin \delta_b]_R k_l(\lambda R) \}. \quad (\text{A24})$$

-
- [1] M. B. Trzhaskovskaya, V. K. Nikulin, and Y. N. Tsarev, *High Energy Density Phys.* **29**, 1 (2018).
- [2] Y. Jian-Min, *Chin. Phys. Lett.* **19**, 1459 (2002).
- [3] A. Goldberg, B. F. Rozsnyai, and P. Thompson, *Phys. Rev. A* **34**, 421 (1986).
- [4] D. Salzmann, R. Y. Yin, and R. H. Pratt, *Phys. Rev. A* **32**, 3627 (1985).
- [5] W. R. Johnson and J. Nilsen, *High Energy Density Phys.* **31**, 92 (2019).
- [6] J. Chluba, A. Ravenni, and B. Bolliet, *Mon. Not. R. Astron. Soc.* **492**, 177 (2020).
- [7] J. Meyer-ter-Vehn and R. Ramis, *Phys. Plasmas* **26**, 113301 (2019).
- [8] G. S. J. Armstrong, J. Colgan, D. Kilcrease, and N. H. Magee Jr., *High Energy Density Phys.* **10**, 61 (2014).
- [9] C. Fortmann, G. Ropke, and A. Wierling, in *16th IEEE International Pulsed Power Conference, Albuquerque, NM* (IEEE, 2007), pp. 194–197.
- [10] B. Wilson, C. Iglesias, and M. Chen, *J. Quant. Spectrosc. Radiat. Transfer* **81**, 499 (2003).
- [11] R. H. Sutherland, *Mon. Not. R. Astron. Soc.* **300**, 321 (1998).
- [12] F. Perrot, *Laser Part. Beams* **14**, 731 (1996).
- [13] M. A. Berkovsky, D. Kelleher, Y. K. Kurilenkov, and M. Skowronek, *J. Phys. B* **26**, 2475 (1993).
- [14] A. Burgess and H. P. Summers, *Mon. Not. R. Astron. Soc.* **226**, 257 (1987).
- [15] M. Nakagawa, Y. Kohyama, and N. Itoh, *Astrophys. J. Suppl. Ser* **63**, 661 (1987).
- [16] M. Lamoureux, R. Cauble, L. Kim, F. Perrot, and R. H. Pratt, *J. Quant. Spectrosc. Radiat. Transfer* **37**, 283 (1987).
- [17] L. A. Collins and A. L. Merts, *J. Quant. Spectrosc. Radiat. Transfer* **26**, 443 (1981).
- [18] S. M. Younger and W. L. Wiese, *J. Quant. Spectrosc. Radiat. Transfer* **22**, 161 (1979).
- [19] I. J. Feng, M. Lamoureux, R. H. Pratt, and H. K. Tseng, *Phys. Rev. A* **27**, 3209 (1983).
- [20] B. F. Rozsnyai, *J. Quant. Spectrosc. Radiat. Transfer* **22**, 337 (1979).
- [21] R. R. Johnston, *J. Quant. Spectrosc. Radiat. Transfer* **7**, 815 (1967).
- [22] P. J. Brussaard and H. C. Vandehulst, *Rev. Mod. Phys.* **34**, 507 (1962).
- [23] W. J. Karzas and R. Latter, *Astrophys. J. Suppl. S.* **6**, 167 (1961).
- [24] I. P. Grant, *Mon. Not. R. Astron. Soc.* **119**, 241 (1958).
- [25] L. C. Biedenharn, *Phys. Rev.* **102**, 262 (1956).
- [26] J. A. Gaunt, *Philos. Trans. R. Soc. London, Ser. A* **229**, 670 (1930).
- [27] H. A. Kramers, *London Edinburgh Dublin Philos. Mag. J. Sci.* **46**, 836 (1923).
- [28] B. L. Henke, E. M. Gullikson, and J. C. Davis, *At. Data Nucl. Data Tables* **54**, 217 (1993).
- [29] J. H. Hubbell and S. M. Seltzer, Tables of x-ray mass attenuation coefficients and mass energy-absorption coefficients, <http://physics.nist.gov/xaamdi>.
- [30] M. P. Desjarlais, J. D. Kress, and L. A. Collins, *Phys. Rev. E* **66**, 025401(R) (2002).
- [31] W. R. Johnson, C. Guet, and G. F. Bertsch, *J. Quant. Spectrosc. Radiat. Transfer* **99**, 327 (2006).
- [32] C. Starrett, *High Energy Density Phys.* **19**, 58 (2016).
- [33] N. Shaffer, N. Ferris, J. Colgan, D. Kilcrease, and C. Starrett, *High Energy Density Phys.* **23**, 31 (2017).
- [34] R. Piron and T. Blenski, *Contrib. Plasm. Phys.* **58**, 30 (2018).
- [35] M. Y. Kuchiev and W. R. Johnson, *Phys. Rev. E* **78**, 026401 (2008).
- [36] W. R. Johnson, *High Energy Density Phys.* **5**, 61 (2009).
- [37] J. M. Ziman, *Principles of the Theory of Solids* (Cambridge University Press, Cambridge, 1964), Chap. 7.
- [38] G. D. Mahan, *Many-Particle Physics* (Plenum, New York, 2000), Chap. 8.
- [39] A. Kritcher, T. Döppner, D. Swift, J. Hawreliak, G. Collins, J. Nilsen, B. Bachmann, E. Dewald, D. Strozzi, S. Felker *et al.*, *High Energy Density Phys.* **10**, 27 (2014).
- [40] T. Döppner, D. C. Swift, A. L. Kritcher, B. Bachmann, G. W. Collins, D. A. Chapman, J. Hawreliak, D. Kraus, J. Nilsen, S. Rothman *et al.*, *Phys. Rev. Lett.* **121**, 025001 (2018).
- [41] D. C. Swift, A. L. Kritcher, J. A. Hawreliak, A. Lazicki, A. MacPhee, B. Bachmann, T. Döppner, J. Nilsen, G. W. Collins, S. Glenzer *et al.*, *Rev. Sci. Instr.* **89**, 053505 (2018).
- [42] S. Zhang, A. Lazicki, B. Militzer, L. H. Yang, K. Caspersen, J. A. Gaffney, M. W. Däne, J. E. Pask, W. R. Johnson, A. Sharma *et al.*, *Phys. Rev. B* **99**, 165103 (2019).
- [43] J. Nilsen, D. Åberg, H. D. Whitley, B. Wilson, L. H. Yang, P. A. Sterne, M. W. Daene, M. E. Martin, S. Zhang, and W. R. Johnson, *High Energy Density Physics* **37**, 100880 (2020).
- [44] Y. T. Lee, *J. Quant. Spectrosc. Radiat. Transfer* **38**, 131 (1987).
- [45] H. A. Scott and S. B. Hansen, *High Energy Density Phys.* **6**, 39 (2010).
- [46] A. Becker, M. Bethkenhagen, C. Kellermann, J. Wicht, and R. Redmer, *Astron. J.* **159**, 149 (2018).
- [47] *DLMF, NIST Digital Library of Mathematical Functions*, edited by F. W. J. Olver, A. B. Olde Daalhuis, D. W. Lozier, B. I. Schneider, R. F. Boisvert, C. W. Clark, B. R. Miller, and B. V. Saunders, <http://dlmf.nist.gov/>, Release 1.0.21 of Dec. 15, 2018.
- [48] E. Lommel, *Studien über die Bessel'schen Funktionen* (B. G. Teubner, Leipzig, 1868).
- [49] E. C. J. von Lommel, *Math. Ann.* **14**, 510 (1879).